

Boundary conditions for stochastic solutions of the convection-diffusion equation

P. Szymczak* and A. J. C. Ladd†

Department of Chemical Engineering, University of Florida, Gainesville, Florida 32611-6005, USA

(Received 28 October 2002; revised manuscript received 27 May 2003; published 11 September 2003)

Stochastic methods offer an attractively simple solution to complex transport-controlled problems, and have a wide range of physical, chemical, and biological applications. Stochastic methods do not suffer from the numerical diffusion that plagues grid-based methods, but they typically lose accuracy in the vicinity of interfacial boundaries. In this work we introduce some ideas and algorithms that can be used to implement boundary conditions in stochastic simulations of the convection-diffusion equation with accuracies comparable to the bulk phase. The algorithms have been tested in two-dimensional channel flows over a range of Peclet numbers, and compared with independent finite-difference calculations.

DOI: 10.1103/PhysRevE.68.036704

PACS number(s): 02.70.Ns, 82.20.Wt, 05.40.Jc, 66.10.Cb

I. INTRODUCTION

The convection-diffusion equation

$$\partial_t c(\mathbf{r}, t) + \mathbf{v}(\mathbf{r}, t) \cdot \nabla c(\mathbf{r}, t) = D \nabla^2 c(\mathbf{r}, t) \quad (1)$$

is the basic transport equation for a wide range of physical, chemical, and biological processes. Here D is the diffusion coefficient and \mathbf{v} is the fluid velocity field, which is taken to be incompressible ($\nabla \cdot \mathbf{v} = 0$). In this work we interpret $c(\mathbf{r}, t)$ as a concentration field, but Eq. (1) may equally well describe heat transfer [1] or the evolution of fluid vorticity [2]. In spite of its relatively simple form, a numerical solution of Eq. (1) can be computationally demanding [3,4]. In particular, a strongly convective flow gives rise to an additional length scale in the vicinity of an interface, which can be difficult to resolve. The thickness of this boundary layer is of the order of $L \text{Pe}^{-1/3}$, where L is the channel width, $\text{Pe} = VL/D$ is the Peclet number, and V is a characteristic velocity of the flow. Peclet numbers for mass transport are typically three orders of magnitude larger than the corresponding Reynolds number of the flow, this being the ratio of the kinematic viscosity of the fluid to the molecular diffusion coefficient. Thus the concentration field near an interfacial boundary varies on a length scale that is an order of magnitude less than the velocity field.

The convection-diffusion equation, Eq. (1), can be solved by finite-element analysis [5], but although very accurate results are possible for diffusion-dominated problems, at high Peclet numbers grid-based methods suffer from numerical dispersion (if upwind differencing is used) or oscillatory and even unstable solutions (if central differencing is used). Although there are methods to circumvent these difficulties [5], their implementation is problematic in complex geometries, where it is difficult to control the potential sources of error. To avoid such problems, Lagrangian particle tracking methods have been frequently used, the most straightforward implementation being the random-walk method [1,2,6–11].

Here the concentration profile is represented by a set of moving particles, which are advected according to the velocity field, while the diffusive displacements of the particles are sampled from a random distribution. Particle-tracking methods are stable, easy to implement, and free of numerical dispersion and grid-generation problems. In this paper we address one of the major difficulties of random-walk methods, namely, the imposition of appropriate boundary conditions on the concentration field.

The other major drawback of a random walk is its stochastic nature, so that the results include statistical errors proportional to $N^{-1/2}$ where N is the number of particles in the simulation. Mixed Euler-Lagrange methods have been proposed to eliminate the statistical errors in random walks, for example the method of characteristics [12–14]. Here the convection term is accounted for by particle tracking while diffusion is taken care of by finite difference. A different approach is taken by the particle-strength-exchange method [15,16], where the differential diffusion operator is replaced by an integral operator that is discretized by using the positions of the particles as quadrature points. The concentration associated with each particle is then modified to account for the diffusion process. In contrast to the method of characteristics, a fixed grid is not needed. Although these schemes generally perform better than finite-difference methods for convection-dominated problems, some implementations of the method of characteristics may lead to artificial oscillations whereas others suffer from numerical dispersion and violation of mass conservation [17]. Particle-strength-exchange methods require frequent remeshing of particle positions, as convection distorts the uniformity of the particle distribution and causes loss of accuracy in the quadratures. This issue becomes more important in highly nonuniform flows or in complex geometries where remeshing may not be straightforward. However, in the computational fluid dynamics community there is a growing consensus in favor of particle-strength-exchange methods [18], based on their efficient representation of fluid vorticity fields. Nevertheless, in this work we will continue to use random walks, because in our applications the convective velocity field is independent of the concentration field c . Thus random errors in concentration are not amplified by correlated errors in velocity as they are in the vortex method. The focus of this paper is on

*On leave from Institute of Theoretical Physics, Warsaw University, 00-681 Hoża 69, Poland.

†Email address: ladd@che.ufl.edu

developing boundary conditions for stochastic solutions of the convection-diffusion equation, but our results may also be applicable to other Lagrangian schemes.

Although stochastic methods can lead to accurate solutions of the convection-diffusion equation in bulk phases, they typically lose accuracy in the region of interfacial boundaries [19]. In this paper we develop boundary conditions for the convection-diffusion equation [Eq. (1)], and consider their spatial and temporal convergence. We focus on the simplest boundary conditions on the concentration field, namely, zero-flux (reflection) and zero-concentration (absorption) interfaces. The absorbing boundary has also been generalized to simulate a finite-concentration reservoir condition. In subsequent work we will consider more general mass-transfer conditions corresponding to complex chemical kinetics at the solid surfaces.

The paper is organized as follows. In Sec. II we summarize basic results concerning stochastic solutions of the convection-diffusion equation. In Sec. III we introduce the different types of boundary conditions and sketch the basic ideas behind their implementation. We then show how the reflection boundary condition can be modified to account for convection near the interface (Sec. IV). In Sec. V we consider the difficulties that occur in implementing an outflow condition. In Sec. VI, additional errors introduced by using non-Gaussian distributions of displacements are analyzed; these are much more severe in the vicinity of the interface than in the bulk. The algorithms are tested using two-dimensional channel flows, for which independent numerical solutions can be computed (Sec. VII), and conclusions are drawn in Sec. VIII.

II. CONVECTION DIFFUSION IN THE BULK

A stochastic process $\mathbf{X}(t)$, associated with the convection-diffusion equation [Eq. (1)], obeys the stochastic differential equation

$$d\mathbf{X} + \mathbf{v}(\mathbf{X})dt = \sqrt{2D}d\mathbf{W}, \quad (2)$$

where $d\mathbf{W}$ is the differential of a Wiener process with unit variance. Stochastic algorithms for the bulk are well developed [19–21], including intricate schemes with higher-order convergence (for a thorough review see Ref. [20]). The simplest numerical approximation to Eq. (2) is the Euler method

$$\mathbf{X}(t + \Delta t) = \mathbf{X}(t) + \mathbf{v}(\mathbf{X}(t))\Delta t + \sqrt{2D}\Delta\mathbf{W}(t), \quad (3)$$

where the increment $\Delta\mathbf{W}(t) = \mathbf{W}(t + \Delta t) - \mathbf{W}(t)$ is a Gaussian random variable with variance Δt . Since we are interested in the evolution of a distribution function rather than individual trajectories, we use the notion of weak convergence [20,21] to characterize the accuracy of a particular numerical scheme. Specifically, an approximation \mathbf{X} is said to be weakly convergent with order ν to the exact solution \mathbf{X}_{ex} if there exists a positive constant δ such that the error in any polynomial function of \mathbf{X} is bounded by

$$|\langle g(\mathbf{X}_{ex}(t)) - g(\mathbf{X}(t)) \rangle| \leq \delta(\Delta t)^\nu \quad (4)$$

for sufficiently small Δt . Global convergence of order ν is guaranteed if the local error at each time step is bounded by [19]

$$|\langle g(\mathbf{X}_{ex}(\Delta t)) - g(\mathbf{X}(\Delta t)) \rangle| \leq \delta(\Delta t)^{\nu+1}. \quad (5)$$

Equation (3) can be proved to be a weakly first-order approximation to the solution of Eq. (2). Higher-order approximations can be constructed along similar lines [20], but these are computationally more complex and expensive. More importantly, the fluid velocity field is usually obtained by some sort of numerical approximation, so that higher derivatives of \mathbf{v} are known with less precision than \mathbf{v} itself. Consequently, most higher-order algorithms are of the predictor-corrector type, the simplest of which is the Heun method, with trajectories constructed according to

$$\begin{aligned} \mathbf{X}(t + \Delta t) = & \mathbf{X}(t) + \frac{1}{2}\{\mathbf{v}(\mathbf{X}(t)) + \mathbf{v}(\mathbf{X}^p(t + \Delta t))\}\Delta t \\ & + \sqrt{2D}\Delta\mathbf{W}(t). \end{aligned} \quad (6)$$

The predictor step for \mathbf{X}^p is an Euler step [Eq. (3)] with the same random increment $\Delta\mathbf{W}(t)$. The Heun method is weakly second order convergent when the diffusion coefficient is independent of spatial position, but higher-order algorithms for spatially varying diffusion coefficients are considerably more complicated [20,21].

Since the velocity field typically changes on much longer length scales than the concentration field, an alternative algorithm can be constructed based on the assumption that the fluid velocity field is locally linear,

$$\mathbf{v}(\mathbf{r}) = \mathbf{v}(\mathbf{r}_0) + (\mathbf{r} - \mathbf{r}_0) \cdot \nabla \mathbf{v}(\mathbf{r}_0). \quad (7)$$

Then in the frame moving with velocity $\mathbf{v}(\mathbf{r}_0)$ tracer particles satisfy the Ornstein-Uhlenbeck equation

$$d\mathbf{X} + \mathbf{X} \cdot \nabla \mathbf{v} dt = \sqrt{2D}d\mathbf{W}, \quad (8)$$

which has an exact solution [22] that can be used as a local approximation to the solution of Eq. (2). On the other hand, the order of convergence of this method for nonlinear flow fields is Δt as opposed to Δt^2 for a second-order Euler or Heun method. In a number of test problems (Sec. VII) the differences between the concentration profiles obtained with the Heun and Ornstein-Uhlenbeck methods were within the range of the statistical errors. Since the Heun method is faster and simpler to implement, we decided to use it in our subsequent simulations.

It has not been possible to extend the Ornstein-Uhlenbeck analysis to include any physically relevant boundary conditions. Nor has it been possible to devise second-order approximations in the presence a general flow field. However, by considering flows that occur under relevant physical conditions we have been able to obtain second-order approximations to the stochastic processes near reflecting and absorbing walls. This has been accomplished for two characteristic flow fields: a linear shear flow, which typifies the flow near a solid interface, and a locally uniform flow, which occurs near an inflow or outflow boundary.

It is frequently argued [19,20] that finite-range increments are preferable to Gaussian distributions in stochastic simulations. They are simpler to generate and avoid the occasional long jumps generated from Gaussian distributions, which may be troublesome in systems of finite size. However, near an interface *any* non-Gaussian increment reduces the order of local convergence to 1/2 [19], and does not guarantee global convergence even in the $\Delta t \rightarrow 0$ limit. In describing our algorithms for imposing boundary conditions on the convection-diffusion equation (Secs. III–V), we will assume that the displacements are being sampled from Gaussian distributions, which simplifies the analysis. Additional errors introduced by finite-range increments will be examined in Sec. VI.

III. BOUNDARY CONDITIONS

We consider a domain \mathcal{V} , bounded by the surface \mathcal{S} , and use a system of units such that the root-mean-square displacement in unit time, $\sqrt{2D}$, is unity. The boundary conditions to be considered in this paper are as follows:

- (1) A zero-flux (reflection) condition:

$$\hat{\mathbf{n}}(\mathbf{r}) \cdot \nabla c(\mathbf{r}) = 0, \quad \mathbf{r} \in \mathcal{S}, \quad (9)$$

where $\hat{\mathbf{n}}(\mathbf{r})$ is a unit vector normal to the surface.

- (2) A constant-concentration boundary condition:

$$c(\mathbf{r}, t) = c_0, \quad \mathbf{r} \in \mathcal{S}. \quad (10)$$

The special case $c_0 = 0$ describes a totally absorbing boundary,

$$c(\mathbf{r}, t) = 0, \quad \mathbf{r} \in \mathcal{S}. \quad (11)$$

In future work we will investigate more complex boundary conditions describing mass transfer due to chemical reactions at the interface:

$$\hat{\mathbf{n}}(\mathbf{r}) \cdot \mathbf{J}_i(\mathbf{r}) = -D_i \nabla c_i(\mathbf{r}) \cdot \hat{\mathbf{n}}(\mathbf{r}), \quad \mathbf{r} \in \mathcal{S}, \quad (12)$$

where \mathbf{J}_i is the flux of species i and depends on the local concentrations.

A. Reflecting wall

In the absence of flow, the Greens function for a reflecting wall situated at $x=0$, G_r , can be constructed by taking the mirror image of the infinite-space propagator [23,24],

$$G(x, x', \Delta t) = \frac{e^{-(x-x')^2/4D\Delta t}}{\sqrt{4\pi D\Delta t}}. \quad (13)$$

In a one-dimensional half space, $x > 0$,

$$G_r(x, x', \Delta t) = G(x, x', \Delta t) + G(x, -x', \Delta t). \quad (14)$$

The mirror symmetry in G_r about the plane $x=0$ ensures that the zero-flux condition is exactly satisfied. A stochastic implementation of the reflecting boundary condition can be realized by a specular reflection of each tracer particle cross-

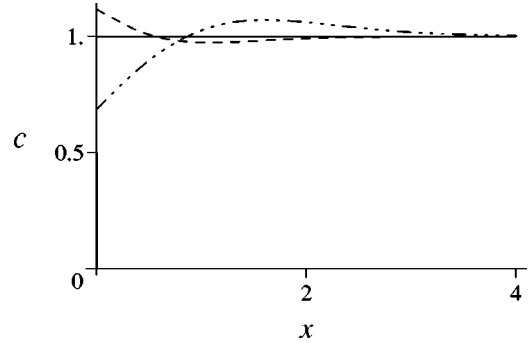


FIG. 1. Comparison of different reflecting boundary algorithms after a single time step: specular reflection and rejection (solid), interruption (dashed), and multiple rejection (dot-dot-dot-dashed). The graphs show concentration profiles $c(x, 1)$ evolving from an initial concentration $c(x, 0) = 1$ with a reflecting wall situated at $x = 0$. The unit of length $\sqrt{2D}$ is the root-mean-square-displacement in unit time.

ing the plane $x=0$. In the general case, a stochastic trajectory $\mathbf{X}(t)$, in the region of a reflecting boundary defined by the local surface normal $\hat{\mathbf{n}}$, evolves according to

$$\mathbf{X}(t + \Delta t) = \mathbf{X}(t) + \Delta \mathbf{W}(t), \quad \mathbf{X}(t) + \Delta \mathbf{W}(t) \in \mathcal{V}$$

$$\mathbf{X}(t + \Delta t) = \mathbf{R} \cdot [\mathbf{X}(t) + \Delta \mathbf{W}(t)], \quad \mathbf{X}(t) + \Delta \mathbf{W}(t) \notin \mathcal{V}, \quad (15)$$

where \mathbf{R} is the mirror reflection operator $\mathbf{R} = \mathbf{1} - 2\hat{\mathbf{n}}\hat{\mathbf{n}}$.

Specular reflection is commonly used for simulating a zero-flux boundary condition [8,18,25], but a number of other methods have also been proposed. For an increment $\Delta \mathbf{W}(t)$ such that $\mathbf{X}(t) + \Delta \mathbf{W}(t) \notin \mathcal{V}$, these include the following.

(1) *Rejection* [26,27]. The particle does not change its position in the given time step, $\Delta \mathbf{W}(t) = 0$.

(2) *Multiple rejection* [28]. New increments are calculated until a $\Delta \mathbf{W}(t)$ is found such that $\mathbf{X}(t) + \Delta \mathbf{W}(t) \in \mathcal{V}$.

(3) *Interruption* [29,30]. The particle stops at the wall and its clock is incremented by $\lambda \Delta t$ with λ given by

$$\mathbf{X}(t + \lambda \Delta t) = \mathbf{X}(t) + \lambda \Delta \mathbf{W}(t). \quad (16)$$

Then, an additional step with $\Delta t' = \Delta t(1 - \lambda)$ is performed.

However, all these schemes fail to impose the zero-flux boundary condition $(\partial c / \partial x)_{x=0} = 0$ correctly, even in the limit of purely diffusive transport. Figure 1 shows that only the specular-reflection and rejection methods preserve an initially uniform distribution; both the multiple-rejection and increment methods distort even the steady-state distribution $c(x) = 1$. In the transient case, shown in Fig. 2, only the specular-reflection method [Eq. (15)] immediately imposes the zero-flux boundary condition; all the other methods lead to incorrect concentration profiles in the immediate vicinity of the interface. Moreover, in higher spatial dimensions, only specular reflection preserves gradients parallel to the surface.

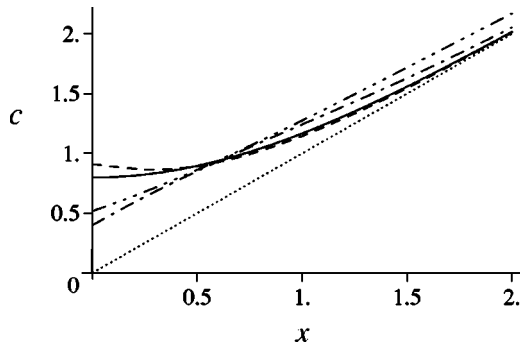


FIG. 2. Comparison of different reflecting boundary algorithms for the initial profile $c(x,0)=x$ (dotted). The graphs show concentration profiles $c(x,1)$ for the following algorithms: specular reflection (solid), interruption (dashed), rejection (dot-dashed), and multiple rejection (dot-dot-dot-dashed).

B. Absorbing wall

An absorbing wall boundary condition

$$c(\mathbf{r})=0, \quad \mathbf{r} \in \mathcal{S} \tag{17}$$

can be implemented in a similar way to the reflecting wall by introducing negative mass particles or holes. The Green function for a particle diffusing in a half space $x>0$, with an absorbing interface at $x=0$, is [23]

$$G_a(x,x',\Delta t)=G(x,x',\Delta t)-G(x,-x',\Delta t), \tag{18}$$

which differs from the reflection propagator [Eq. (14)] in the sign of the second term. It is simpler to add a distribution of holes to account for the negative sign, rather than attempt to remove a distribution of particles. Thus we implement the absorbing boundary condition by reflecting particles at the plane $x=0$ and then converting them into holes. Similarly, holes that attempt to recross the boundary are reflected and converted back into particles.

Other methods for simulating a zero-concentration boundary condition are found in the literature, typically the “total absorption” method [6,31,32], where particles are removed when $\mathbf{X}(t)+\Delta\mathbf{W}(t)$ lies outside the domain \mathcal{V} . However, in this case the plane of zero concentration is shifted outside the system by a distance of order of the mean-square displacement $\sqrt{2D\Delta t}$ (see Figs. 3 and 4). On the other hand, the “reflection-conversion” scheme ensures that the concentration is exactly zero on the absorbing wall, regardless of the time step Δt . The total absorption method can be corrected by removing additional particles near the wall [19], but this is more complicated than reflection conversion.

C. Contact with particle reservoir

A reservoir boundary condition of constant concentration $c(0)=c_0$ can be imposed by combining reflection conversion (Sec. III B) with a virtual concentration profile behind the interface. In the absence of convection it can be shown that the virtual distribution

$$c_v(x)=2c_0, \quad x<0 \tag{19}$$

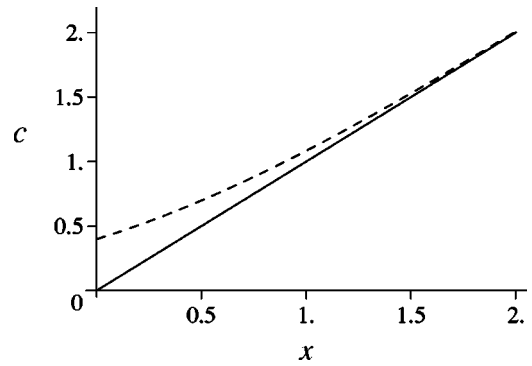


FIG. 3. Simulation of a zero-concentration boundary condition: reflection-conversion (solid) and absorption (dashed). The graphs show the concentration profiles $c(x,1)$ after a single time step, beginning with a profile $c(x,0)=x$. For the reflection-conversion scheme the concentration profile is stationary, while for the absorption scheme the zero-concentration boundary condition is not preserved.

produces a concentration profile in the system ($x>0$)

$$c(x,\Delta t)=c_0 \left[1 - \text{Erf} \left(\frac{x}{\sqrt{4D\Delta t}} \right) \right] \tag{20}$$

after a time Δt . Equation (20) is a solution of the one-dimensional diffusion equation, with boundary conditions $c(0)=c_0$ and $c(x\rightarrow\infty)=0$. Reflection conversion ensures that the real distribution ($x>0$) satisfies the one-dimensional diffusion equation, with a boundary condition $c(0)=0$. Thus in combination, the real and virtual particles lead to precisely the correct boundary condition, at least in one dimension.

D. Particle-hole recombination

The algorithm described in Sec. III B introduced the concept of holes or particles with negative mass. As far as the numerical simulation is concerned, a hole behaves just like a particle; it moves according to the same propagator G , specularly reflects off a reflecting wall, and after reflecting

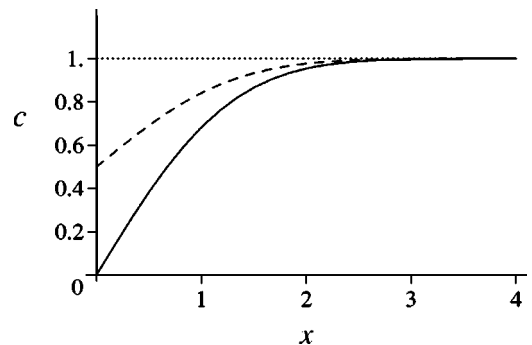


FIG. 4. Simulation of a zero-concentration boundary condition with an initial profile $c(x,0)=1$ (dotted). The graphs show the concentration profiles $c(x,1)$ after a single time step. Again, only the reflection-conversion scheme (solid) assures that $c(0,t)=0$; the absorption method (dashed) leads to a nonzero concentration at the surface.

off an absorbing wall becomes a particle again. However, the introduction of holes has the drawback that the local concentration can become a small difference between large populations of particles and holes. Statistical errors in the concentration field can be reduced by canceling equal numbers of particles and holes within the same small volume in the bulk. It is important to avoid any bias or spatial correlations in this process.

Recombination of particles and holes can be implemented by dividing the domain \mathcal{V} into a number of nonoverlapping cells C_i , typically small cubic volume elements. The number of particles and holes contained in C_i is denoted by p_i and h_i , respectively. Recombination consists of randomly picking $n_i = \min(p_i, h_i)$ particles and n_i holes from C_i , and erasing them. The procedure is repeated in each cell. If the dimensions of the cells are sufficiently small, much smaller than any characteristic length scale in the simulation (including the root-mean-square displacement of the random walk), the effect of recombination on the distribution $c(\mathbf{r}, t)$ will be negligible. The recombination is performed every R time steps, where R should be neither too small (to ensure a reasonable number of holes before recombination) nor too large so that the statistical errors accumulate. In practice it is straightforward to keep the particle and hole population steady while not losing significant information about the concentration profile.

IV. ZERO-FLUX BOUNDARY CONDITION

We begin our analysis of the convection-diffusion problem with a two-dimensional system confined to the $x > 0$ half space by a reflecting wall situated at $x = 0$. The no-slip boundary condition on the solid surface, $\mathbf{v}(\mathbf{r} \in \mathcal{S}) = \mathbf{0}$, allows for significant simplification if we restrict the time step Δt so that the fluid velocity field near the wall varies linearly over a typical particle displacement. Assuming the fluid is incompressible, then to a first approximation the velocity field is tangential to the surface and linear in the normal distance from the surface. With an appropriate choice of a coordinate system, the velocity field near the wall can therefore be written as

$$\mathbf{v}(x, y) = x\gamma\mathbf{e}_y + \dots \quad (21)$$

Thus the problem is reduced to the solution of a two-dimensional convection-diffusion equation in a linear shear flow

$$\frac{\partial c(x, y)}{\partial t} + \gamma x \frac{\partial c(x, y)}{\partial y} = D \left(\frac{\partial^2 c(x, y)}{\partial x^2} + \frac{\partial^2 c(x, y)}{\partial y^2} \right), \quad (22)$$

with the boundary condition

$$\left(\frac{\partial c(x, y)}{\partial x} \right)_{x=0} = 0. \quad (23)$$

In the absence of convection, the reflection Green's function is constructed from the infinite-space solution by intro-

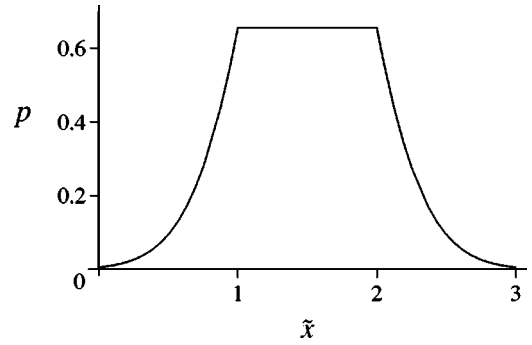


FIG. 5. The conditional probability distribution $p(\tilde{x}|x, x', \Delta t)$ for a trajectory beginning at $x' = 1$ and ending at $x = 2$ after unit time $\Delta t = 1$ [Eq. (25)].

ducing an image source on the opposite side of the boundary [Eq. (14)]. However, in a shear flow the image of the Ornstein-Uhlenbeck process is not a solution of the original convection-diffusion equation (22), but of that with the sign of the shear rate, γ , reversed. Thus we cannot construct the equivalent stochastic process by combining an Ornstein-Uhlenbeck process with its image. Nevertheless, the idea of reflecting the particle position with respect to the wall can be implemented within a predictor-corrector scheme to maintain second-order accuracy, even near the interface. We observe that the normal (x) displacement has no convective component and is therefore independent of position in the vicinity of the interface. Thus a random displacement with reflection is sufficient to give an exact sampling of the normal motion. In order to determine the convective contribution to the tangential (y) displacement we must integrate over all possible trajectories between the initial and final x positions. In the bulk this gives the linearly averaged velocity used in the Heun method [Eq. (6)], but near the interface, the weighting function is different. To obtain the proper weighting function in this case, we must calculate the mean time the particle spends at a position \tilde{x} during its move from x' to x in the time step Δt :

$$p(\tilde{x}|x, x', \Delta t)\Delta t = \frac{\int_0^{\Delta t} G(x, \tilde{x}, \Delta t - t)G(\tilde{x}, x', t)dt}{G(x, x', \Delta t)}, \quad (24)$$

where $G(x, x', t)$ is the one-dimensional diffusion propagator, Eq. (13). The integral in Eq. (24) can be calculated using Laplace transforms:

$$p(\tilde{x}|x, x', \Delta t) = \frac{1}{4D\Delta t G(x, x', \Delta t)} \operatorname{Erfc} \left(\frac{|\tilde{x} - x| + |\tilde{x} - x'|}{\sqrt{4D\Delta t}} \right), \quad (25)$$

and this probability distribution is illustrated in Fig. 5. Interestingly it is uniform between x and x' , with tails accounting for the paths that move outside the interval (x, x') .

The average convective velocity in the time step Δt can be calculated by integrating the flow field at each \tilde{x} with $p(\tilde{x}|x,x',\Delta t)$ as the weight function:

$$\bar{v}_y = \gamma \int_{-\infty}^{\infty} \tilde{x} p(\tilde{x}|x,x',\Delta t) d\tilde{x} = \gamma f(x,x'). \quad (26)$$

The paths described by \tilde{x} may extend into the virtual region $\tilde{x} < 0$. Physically, the particle is reflected and remains in the real ($\tilde{x} > 0$) domain, but it is simpler computationally to allow negative values of \tilde{x} and change the sign of the shear rate. In calculating the mean convective velocity we must also differentiate between situations where the final point x is reached directly and where it is reached after reflection. Since p is translationally invariant, it is the displacement $x - x'$, along with the time step Δt , that are the controlling parameters in p . Therefore, the final position x in Eqs. (24)–(26) must be calculated without reflection, and can be positive or negative. If the particle is far from the wall, the averaged velocity is, by symmetry, $\gamma(x+x')/2$ as used in the Heun method [Eq. (6)]. However, as the particle comes close to the wall, the tails in the distribution become more important, especially when $|x-x'| \ll \sqrt{D\Delta t}$. For example, if $x = x' = 0$ and $D\Delta t = 1$, the particle attains an average velocity of about 0.3γ .

These ideas can be implemented by modifying the Heun method [Eq. (6)] whenever there is a significant probability that the particle trajectory explores the virtual region behind the interface. In such cases the convective increment in the corrector step should be weighted according to Eq. (26). The velocity field near the wall can be used to estimate the magnitude and direction of the local shear rate $\bar{\gamma}$, and the new particle position is then given by

$$\mathbf{X}(t+\Delta t) = \mathbf{R} \cdot [\mathbf{X}(t+\Delta t) + \bar{\gamma} f(\mathbf{X}^p(t+\Delta t) \cdot \hat{\mathbf{n}}, \mathbf{X}(t) \cdot \hat{\mathbf{n}}) \Delta t + \sqrt{2D\Delta t} \mathbf{W}(t)], \quad (27)$$

where $f(x,x')$ is calculated from Eq. (26). It should be noted that \mathbf{X}^p is calculated without the reflection operator and may lie outside the system; this point was discussed in the text following Eq. (26).

If the velocity field has the form of a shear flow [Eq. (21)] everywhere, not only in the vicinity of the wall, then the above algorithm is equivalent to advancing the concentration profile with the approximate reflection propagator:

$$G(x,x',y,y',\Delta t) = \frac{1}{4\pi D\Delta t} \left(\exp \left[-\frac{(x-x')^2 + [y-y' + \gamma f(x,x')\Delta t]^2}{4D\Delta t} \right] + \exp \left[-\frac{(x+x')^2 + [y-y' + \gamma f(x,-x')\Delta t]^2}{4D\Delta t} \right] \right). \quad (28)$$

Although it is not an exact solution of the convection-diffusion equation, the proposed algorithm guarantees that a

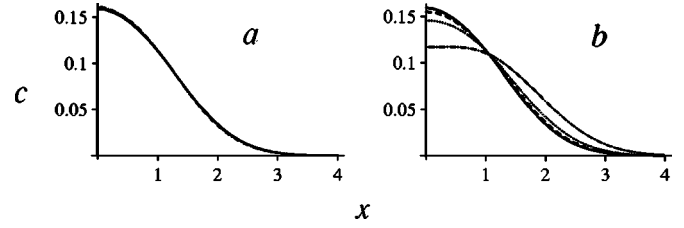


FIG. 6. Convection diffusion near a planar reflecting boundary ($x=0$) in the presence of a linear shear flow. A point source is placed at $(1,0)$ and the time evolution is simulated using specular reflection at the solid boundary: (a) second-order predictor-corrector method, Eq. (27); (b) first-order Euler method with specular reflection. The concentration profiles at $t=1$, $c(x,0,1)$, obtained with time steps $\Delta t=1$ (dot-dashed), $\Delta t=1/3$ (dotted), and $\Delta t=1/10$ (dashed), are compared with the exact solution (solid).

zero-flux boundary condition $\hat{\mathbf{n}} \cdot \nabla c = 0$ is maintained at the boundary regardless of the time step. This can be checked by direct differentiation of the Green function (28) and using the symmetry relations $f(0,x') = f(0,-x')$ and $\partial_x f(0,x') = -\partial_x f(0,-x')$.

To test the algorithms, we simulated a random walk in a linear shear flow $v_y = x$, near a reflecting wall at $x=0$, starting from an initial δ -function distribution

$$c(x,y,0) = \delta(x-1)\delta(y). \quad (29)$$

As there is no analytical solution of the problem, results were compared with a numerical approximation to the exact solution, obtained by releasing a large number ($N=10^7$) of tracer particles and advecting them with a very small time step ($\Delta t=10^{-5}$). Figure 6(a) compares the concentration profile calculated using our predictor-corrector algorithm, with the “exact” numerical solution. The predictor-corrector algorithm is rapidly convergent, consistent with second-order accuracy, and results obtained with $\Delta t < 0.5$ are indistinguishable from the exact profile on the scale of the figure. By comparison, Fig. 6(b) shows analogous results obtained with a first-order Euler algorithm, including specular reflection whenever the trajectory crosses the interface. It can be seen that the errors are larger and the convergence is more or less linear. Figure 7 shows that the interruption and multiple-rejection methods have larger errors than the Euler method and that the concentration profile converges to the wrong result in the vicinity of the source point. Such algorithms

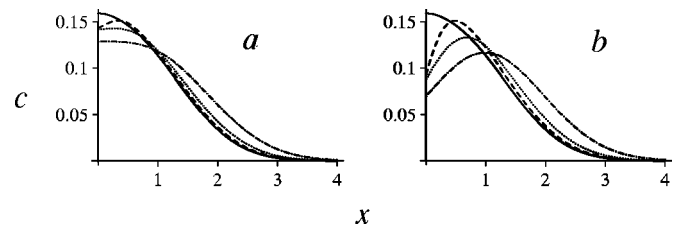


FIG. 7. Convection diffusion near a planar reflecting boundary is simulated using (a) interruption and (b) multiple-rejection methods. The concentration profiles at $t=1$, $c(x,0,1)$, obtained with time steps $\Delta t=1$ (dot-dashed), $\Delta t=1/3$ (dotted), and $\Delta t=1/10$ (dashed), are compared with the exact solution (solid).

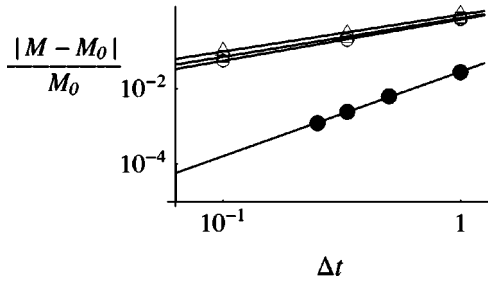


FIG. 8. Differences between the second moment of the concentration profiles in Figs. 6 and 7 and the second moment of the exact concentration profile, M_0 . The predictor-corrector algorithm (solid circles) shows quadratic convergence (slope 2.2 ± 0.2), while the other methods converge linearly. These methods are Euler (open circles), interruption (open squares), and multiple rejection (open triangles).

cannot generate the correct Green function for the convection-diffusion equation, even with very small time steps.

Despite the relatively large errors in concentration, the moments of the distribution calculated by interruption and multiple rejection converge linearly with the time step, as shown in Fig. 8. The errors in the second moment are comparable to the Euler method, which also converges linearly with Δt . The predictor-corrector method has much smaller errors and converges quadratically with Δt .

V. DIRICHLET BOUNDARY CONDITIONS

The most important example of Dirichlet boundary conditions is an absorbing boundary

$$c(\mathbf{r}, t) = 0, \quad \mathbf{r} \in \mathcal{S}, \quad (30)$$

where the concentration vanishes. In Sec. III B we showed that the Green function for diffusion near an absorbing wall could be interpreted using particles of negative mass (holes), which enter the system with trajectories that mirror those of real particles leaving the system. A zero-concentration (absorbing) boundary condition can be implemented by modifying the predictor-corrector scheme of Sec. IV so that reflected particles are converted into holes, carrying negative mass in the overall concentration balance. This algorithm ensures that the concentration on the wall vanishes regardless of the time step used in a random walk (Fig. 9), and is second-order convergent in time.

Outflow boundary condition

It is often the case that a zero-concentration condition is imposed on some imaginary surface in the fluid, for example, at an inlet or outlet, rather than on a solid wall. In this case the fluid velocity does not vanish at the boundary, but to leading order the velocity field can be taken to be constant,

$$\mathbf{v}(x, y) = \mathbf{v}^0 + \dots \quad (31)$$

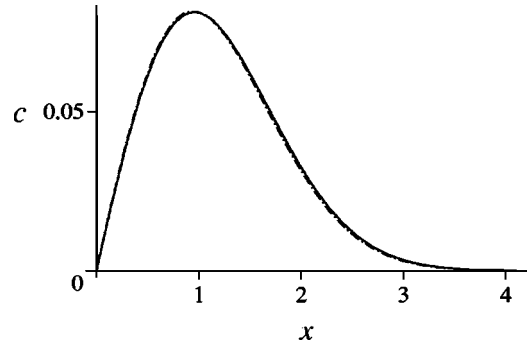


FIG. 9. Convection diffusion near a planar absorbing boundary ($x=0$) in the presence of a linear shear flow. A point source is placed at the point (1,0) and the time evolution is simulated using reflection conversion at the solid boundary with the second-order convective correction, Eq. (27). The concentration profiles $c(x, 0, 1)$ obtained with time steps $\Delta t = 1$ (dot-dashed), $\Delta t = 1/3$ (dotted), and $\Delta t = 1/10$ (dashed) are compared with the exact solution (solid line).

The Green function in a constant flow field \mathbf{v}^0 is simply

$$G(x, y, x', y', \Delta t) = \frac{1}{4\pi D \Delta t} \exp\left[-\frac{(x-x' - v_x^0 \Delta t)^2 + (y-y' - v_y^0 \Delta t)^2}{4D \Delta t}\right], \quad (32)$$

and without loss of generality, the boundary surface can be taken to be the plane $x=0$. As in the case of pure diffusion, a Green's function for an absorbing wall can be constructed using an image source of negative mass. For a constant flow, Eq. (18) takes the more general form

$$G_a(x, y, x', y', \Delta t) = G(x, y, x', y', \Delta t) - a(x') G(x, y, -x', y', \Delta t), \quad (33)$$

where $a(x')$ can be interpreted as the mass of the hole, which is now variable. The absorption condition $G_a(0, y, x', y', \Delta t) = 0$ requires that

$$a(x') = \frac{G(0, y, x', y', \Delta t)}{G(0, y, -x', y', \Delta t)} = \exp\left[-\frac{x' v_x^0}{D}\right]. \quad (34)$$

We note that in order for Eq. (33) to obey the convection-diffusion equation, $a(x')$ must be independent of the time step Δt , as is the case here.

For the purely diffusive case the Green function [Eq. (18)] was simulated by reflecting particles at the wall and converting them into holes of equal mass, but in the presence of a velocity field, reflection conversion will not apply the correct convective displacement to the holes. Instead we introduce a distribution of virtual holes in the region $x < 0$, outside the system. We have devised two algorithms; the first illustrates the basic idea, the second is a much more efficient implementation.

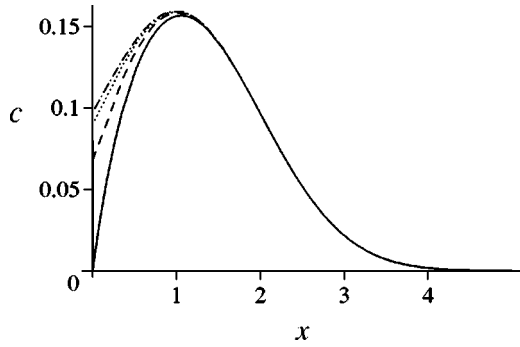


FIG. 10. Evolution of an initial concentration profile $c(x,y,0) = \delta(x-1)\delta(y)$ in a constant flow field $\mathbf{v}=(-1,0)$ with an absorbing wall at $x=0$. Absorption is simulated by the particle removal method. The concentration profiles $c(x,0,1)$, obtained for time steps $\Delta t=1$ (dot-dashed), $\Delta t=1/3$ (dotted), and $\Delta t=1/10$ (dashed), are shown together with the exact solution (solid) given by the Green function (33).

Algorithm I

(1) Make a virtual distribution $c^*(x<0)$ of holes that images the positions of real particles in the region ($x>0$) near the wall: for each particle p_i we create a hole h_i in the position

$$x_{h_i} = -x_{p_i}, \tag{35}$$

$$y_{h_i} = y_{p_i}, \tag{36}$$

behind the wall. The mass of the hole is given by $m_{h_i} = a(x_{p_i})$ and counts $-a(x_{p_i})$ in the overall concentration balance.

(2) Move both virtual holes and real particles according to their infinite-space propagators, keeping only the particles that remain in the system at the end of the time step.

The algorithm ensures that the concentration is exactly zero on the absorbing wall, regardless of the time step Δt , which is not true of a rudimentary alternative [6,32], where particles are removed when their trajectories cross the boundary of the system. Figure 10 shows that particle removal is inaccurate in the vicinity of the wall, even for relatively small time steps.

The outflow condition can also be extended to impose a reservoir boundary condition. An additional distribution of virtual particles is inserted in the region $x<0$ behind the boundary, with a uniform number density $n_p=c_0$, but with a nonuniform mass [cf. Eq. (19)],

$$m_{p_i} = 1 + a(-x_{p_i}). \tag{37}$$

When this distribution is advected, it leads to a concentration profile in the system [cf. Eq. (20)],

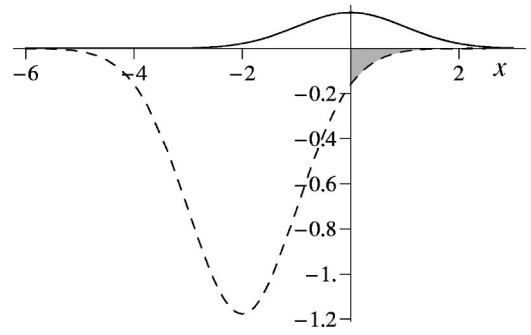


FIG. 11. The positive (solid) and negative (dashed) components of the Green function given by Eq. (33) for $v_0=(-1,0)$, $\Delta t=1$, $x'=1$, and $y'=y=0$. Only a small portion of the negative component (shaded region) enters the real space.

$$c(x,\Delta t) = \frac{c_0}{2} \left[1 + \text{Erf} \left(\frac{v_x^0 \Delta t - x}{\sqrt{4D\Delta t}} \right) \right] + \frac{c_0}{2} \exp \left(\frac{v_x^0 x}{D} \right) \left[1 - \text{Erf} \left(\frac{v_x^0 \Delta t + x}{\sqrt{4D\Delta t}} \right) \right], \tag{38}$$

which is a solution of the convection-diffusion equation with boundary condition $c(0)=c_0$. It is worth noting that in a uniform system, for which $c(x)=c_0$ everywhere in the $x>0$ half space, the total virtual concentration (particles +holes) for $x<0$ will be also constant and equal c_0 . Moreover, in the absence of flow Eq. (19) is recovered, with $a(-x_{p_i})=1$.

Although Algorithm I is exact for constant velocity flows, it becomes inefficient for large negative values of v_x^0 , corresponding to fast outflow of material from the system. Figure 11 shows the characteristic positive and negative components of the Green function [Eq. (33)] in such cases. It can be seen that the negative component, corresponding to the hole distribution, can be orders of magnitude larger than the positive one. At the same time only the very tail of the hole distribution enters the $x>0$ region, so that most of the virtual holes do not enter the system. But whenever one of the holes does cross the $x=0$ plane, it brings a substantial negative mass into the system ($e^{-x_{p_i}v_x^0/D} \gg 1$), which leads to large statistical fluctuations in the concentration field near the boundary.

We therefore propose the following improvement.

Algorithm II

(1) Again create holes at $x_{h_i} = -x_{p_i}$, this time with unit mass $m_{h_i}=1$.

(2) Calculate the probability p_{h_i} that the hole h_i enters the system in the next time step Δt . This corresponds to the area of the shaded region in Fig. 11 and is given by

$$p_{h_i} = \int_0^\infty dx \int_{-\infty}^\infty dy a(x_{p_i}) G(x,y,-x_{p_i},y_{p_i},\Delta t) = \frac{1}{2} e^{-x_{p_i}v_x^0/D} \left[1 + \text{Erf} \left(\frac{\Delta t v_x^0 - x_{p_i}}{\sqrt{4D\Delta t}} \right) \right]. \tag{39}$$

It may be shown by rearranging the integrand in Eq. (39) that p_{h_i} is always less than unity.

(3) With probability p_{h_i} , insert the hole into the system at the point x , sampled from a Gaussian tail distribution that is limited to the region $x > 0$:

$$p(x, y) = \frac{1}{p_{h_i}} a(x_{p_i}) G(x, y, -x_{p_i}, y_{p_i}, \Delta t). \quad (40)$$

Otherwise discard the hole.

This algorithm gives the same concentration profiles as Algorithm I but is much more efficient. Keeping the mass of the hole unitary greatly reduces the statistical fluctuations in $c(x)$ near the boundary.

VI. FINITE-RANGE PROPAGATORS

It is not necessary that $\Delta \mathbf{W}$ be a Gaussian propagator in order to obtain weak convergence. For example, any random variable $\langle \Delta \mathbf{Y} \rangle$ with the correct second moment, i.e.,

$$\begin{aligned} \langle \Delta Y_i \rangle &= 0, \\ \langle \Delta Y_i \Delta Y_j \rangle &= \Delta t \delta_{ij}, \\ \langle \Delta Y_i \Delta Y_j \Delta Y_k \rangle &= 0, \end{aligned} \quad (41)$$

guarantees weak first-order convergence of the approximation scheme [21]. Finite-range increments obeying these moment conditions [Eq. (41)] are frequently used [1,29,30] because these are simpler and faster than Gaussian-sampled increments, and do not introduce significant errors in the bulk. However, near an interface odd moments of the increments are nonzero and space dependent. Reflection propagators constructed from finite-range increments via Eq. (14) or Eq. (27) then have a local error in the first moment proportional to $\Delta t^{1/2}$ [19], which suggests that the global error [Eq. (4)] may not vanish with decreasing time step. However, although the short-time evolution may be poorly convergent, after a sufficiently long time the concentration distribution can still reach the correct steady-state. For example, in the absence of flow it is straightforward to prove that the stationary state of any isotropic propagator is a solution of the Laplace equation. If this propagator can be supplemented with an algorithm that imposes the correct boundary conditions then the errors will decrease with time rather than increase as might be expected in the worst-case scenario.

Even in convection-diffusion problems, finite-range propagators can lead to reasonable results after a few time steps. Figure 12 shows results obtained with a displacement that is sampled uniformly over the surface of a circle, and can be compared with the result for a Gaussian propagator shown in Fig. 6(b). For more than two steps, the errors are similar to those obtained with Gaussian displacements.

Although it is possible to construct practical boundary conditions with finite-range increments, these are nevertheless less accurate and less flexible than Gaussian increments and also more difficult to analyze. To avoid the complications associated with the infinite range of Gaussian propaga-

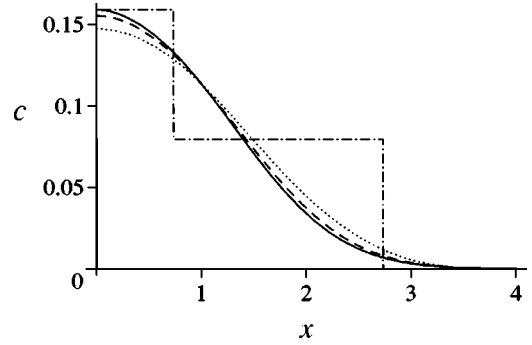


FIG. 12. Convection diffusion near a planar reflecting boundary is simulated using finite-range displacements, distributed uniformly over the area of a circle. The Euler method with specular reflection is used to integrate the stochastic differential equations. The concentration profiles $c(0, y, 1)$ obtained for time steps $\Delta t = 1$ (dot-dashed), $\Delta t = 1/3$ (dotted), and $\Delta t = 1/10$ (dashed) are compared with the exact solution (solid).

tors it may prove advantageous to sample diffusive increments from truncated Gaussian distributions, $p(\Delta W_i / \sqrt{\Delta t}, x_T)$, instead

$$p(x, x_T) = e^{-x^2/2} [A(x_T) + B(x_T)x^2 + C(x_T)x^4]. \quad (42)$$

The coefficients $A-C$ can be constructed to match the zeroth, second, and fourth moments of the Gaussian distribution, although for truncation ranges $x_T < 3\sqrt{\Delta t}$ it is only practical to match the first two nonzero moments. Although for sufficiently small Δt such distributions ultimately have the same convergence properties as any finite-increment distribution, the errors introduced by ignoring the tails of the Gaussian are negligible for sufficiently large x_T . Figure 13 shows the concentration profile for different truncation distances; for $x_T > 3\sqrt{\Delta t}$, the dynamics of the random walk are not noticeably affected.

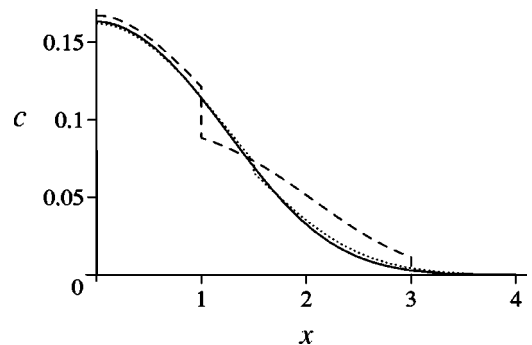


FIG. 13. Convection diffusion near a planar reflecting boundary is simulated using a Gaussian propagator truncated at $2\sqrt{\Delta t}$ (dashed) and at $2.5\sqrt{\Delta t}$ (dot-dashed). The Heun method with specular reflection is used to integrate the stochastic differential equations. The concentration profiles $c(0, y, 1)$ are compared with the exact solution (solid). The results for truncation distances larger than $3\sqrt{\Delta t}$ are indistinguishable on the scale of the figure from those obtained with a Gaussian distribution.

VII. CONVECTION DIFFUSION IN A RECTANGULAR CHANNEL

In this paper we have constructed a set of algorithms that impose reflection (zero-flux) and absorption (zero-concentration) boundary conditions at solid interfaces. In addition we have developed reservoir boundary conditions for the inlets and outlets to the system. Here the algorithms are tested on two-dimensional convection-diffusion problems whose solution can be found independently. We take a channel of width $L_y=10$ and length $L_x=nL_y$, with a constant-concentration inlet $c(0,y,t)=1$ and a zero-concentration outlet $c(L_x,y,t)=0$. The solid wall at $y=0$ is reflecting, $\partial_y c(x,0,t)=0$, and the wall at $y=L_y$ is absorbing, $c(x,L_y,t)=0$. This problem geometry allows us to test all of the types of boundary condition in a single test problem. The tests were run from the diffusion-dominated limit $Pe=0.1$ to the convection-dominated limit $Pe=1000$, using increasing channel lengths at higher Peclet numbers so that the time step can remain constant. The Peclet number $Pe=VL_y/D$ is defined in terms of the velocity at the center of the channel. We have assessed the convergence of the concentration flux at the absorbing wall based on comparisons with a multi-grid finite-difference code from the NAG library [33]. We used a modest aspect ratio grid, at most 2:1, since noticeable errors were observed with high aspect ratios (>10).

The algorithms of Secs. IV and V can be combined in the vicinity of corners where surfaces with two different boundary conditions meet. In such cases we track the motion of the particle, applying the appropriate rules at each successive encounter with a bounding surface. To gain more insight into how and why this works in practice, consider a purely diffusive process in a wedge $x>0,y>0$, bounded by reflecting ($y=0$) and absorbing ($x=0$) walls. For a point source at (x',y') , the reflecting wall adds an image source at $(x',-y')$, while the absorbing wall adds a sink at $(-x',y')$ (see Fig. 14). Near the corner, there is an additional sink at $(-x',-y')$, because of the interaction between reflecting and absorbing boundaries. Thus the Green function is given by

$$G^c(x,y,x',y') = G(x,y,x',y') + G(x,y,x',-y') - G(x,y,-x',y') - G(x,y,-x',-y'). \tag{43}$$

Analogous constructions can be made for other types of corners.

The implementation of Eq. (43) may be achieved in a variety of ways. For example, the image particles and holes can be placed in the appropriate locations and propagated for Δt , retaining only the particles within the system at the end of the time step. However, it is simpler and more effective to move the original particle and perform a specular reflection at the reflecting wall and reflection conversion at the absorbing one (see Fig. 14). Unfortunately, this method only works when there is no flow across the absorbing interface; a flow field introduces an asymmetry in the distribution, so that holes generated by reflection conversion do not have the right convective displacement. Therefore we use an image

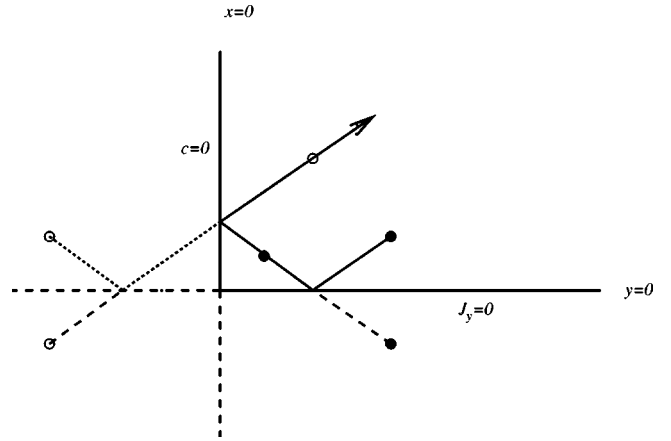


FIG. 14. Diffusion near a corner bounded by reflecting and absorbing walls. In the absence of flow, boundary conditions can be imposed by reflecting the particle at each wall and converting it to a hole when necessary (solid line). However, when there is a flow across the interface, reflection conversion does not sample the correct convective displacement. Instead, the image hole at $(-x',y')$ must be introduced (see Sec. V) and propagated (dotted lines). Both the particle and the hole are allowed to cross the $x=0$ plane but after one time step only the particles inside the wedge ($x>0,y>0$) are retained.

hole at $(-x',y')$ to impose a zero-concentration condition at $x=0$. The hole is moved according to Algorithm I or II, as described in Sec. V. However, the reflecting boundary can always be implemented by specular reflection, so that there is no need to introduce a hole at $(-x',-y')$ or a particle at $(x',-y')$.

The results in Figs. 15–17 show that the stochastic simulations are in essentially exact agreement with the finite-difference results over most of the channel, regardless of the Peclet number. However, there is a singularity in the flux at the corner ($x=0,y=0$), where the boundary conditions $c=1$ (along $x=0$) and $c=0$ (along $y=0$) meet. Here the time step must be reduced to obtain accurate results, particularly at the highest Peclet number (Fig. 17).

Sampling errors can be controlled by increasing the density of particles, N , or by time averaging over an interval T . Figure 18 illustrates the behavior of the statistical errors in

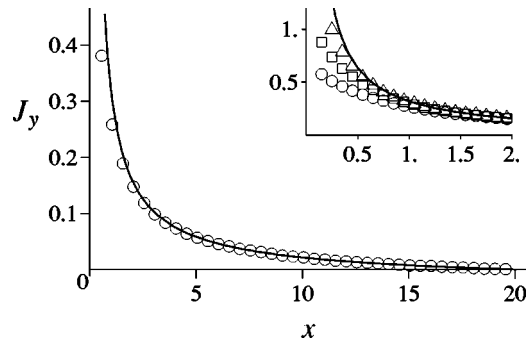


FIG. 15. The flux of particles across an absorbing wall at a Peclet number $Pe=0.1$, as a function of the position along the channel. Random walk simulations (open circles) with a time step $\Delta t=1$ are compared with finite-difference results (solid line). The inset shows results near the inlet position for time steps $\Delta t=1$ (circles), $\Delta t=1/3$ (squares), and $\Delta t=1/10$ (triangles).

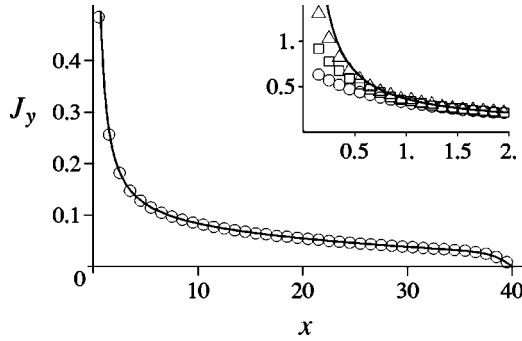


FIG. 16. The flux of particles across an absorbing wall at a Peclet number $Pe=10$, as a function of the position along the channel. Random-walk simulations (open circles) with a time step $\Delta t=1$ are compared with finite-difference results (solid line). The inset shows results near the inlet position for time steps $\Delta t=1$ (circles), $\Delta t=1/3$ (squares), and $\Delta t=1/10$ (triangles).

the particle current at an absorbing interface ($y=0$). The current measured by the random-walk method at different locations, J_i , was compared with the corresponding finite-difference results J_i^{fd} at 30 locations far from the singular entry point, $L_x/4 < x_i < L_x$. The root-mean-square deviation

$$\delta = \sqrt{\frac{\sum_i (J_i - J_i^{fd})^2}{\sum_i (J_i^{fd})^2}} \quad (44)$$

was calculated at a Peclet number $Pe=10$ with a time step $\Delta t=0.1$, and decays as \sqrt{NT} with a coefficient of order 10.

In this work we used long runs to obtain very precise data, and each channel flow simulation ran for ≈ 1 h, whereas the finite-difference code ran for only a few seconds. However, in more complicated geometries we expect statistical errors of the order of 5% to be adequate, and in this case the comparison is more favorable. Moreover, the stochastic simulations evolved in time to a steady state, whereas the finite-difference code solved the time-independent problem

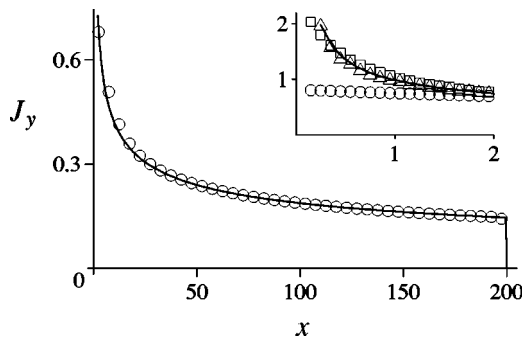


FIG. 17. The flux of particles across an absorbing wall at a Peclet number $Pe=1000$, as a function of the position along the channel. Random-walk simulations (open circles) with a time step $\Delta t=1$ are compared with finite-element results (solid line). The inset figure shows results near the inlet position for time steps $\Delta t=1$ (circles), $\Delta t=1/10$ (squares), and $\Delta t=1/100$ (triangles).

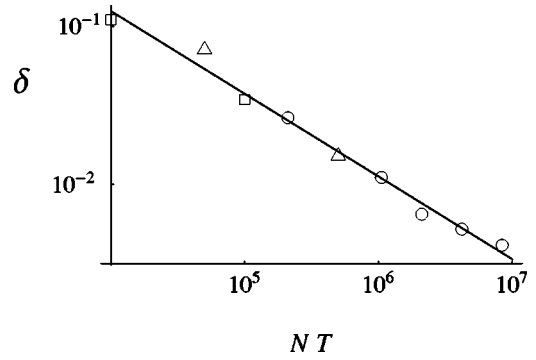


FIG. 18. The statistical error of the measured particle current through absorbing wall as a function of number of time steps, T , over which the measurement is averaged (circles) and the number of particles, N , used to simulate the concentration c_0 in a unit cell (squares). The reference values are $T=21\,000$ and $N=1000$. The slope of the line is -0.52 ± 0.07 indicating square-root convergence characteristic for stochastic methods.

directly. A better comparison would be to estimate the time taken to update the concentration profile for a unit time. From the data shown in Fig. 18 we expect that densities of the order of 10^5 particles per unit area (or volume in the three-dimensional case) will be sufficient to calculate the flux over a unit surface length (or area) to about 3% precision in a single configuration. For the $Pe=10$ simulation this corresponds to a total of about 4×10^7 particles and a single time step would be sufficient to update the system for a unit time. With our current and by no means optimized code, we can update about 10^6 particles per second, so a single step would take of the order of 40 s.

VIII. CONCLUSION

In this paper we have developed and tested stochastic algorithms to solve the convection-diffusion equation in the vicinity of reflecting and absorbing boundaries. The key ideas were the introduction of particles with negative mass (holes) to account for deposition fluxes, and methods to incorporate convection in the vicinity of an interface. In the case of a shear flow we have shown how to correctly sample the distribution of convective velocities to obtain second-order convergence, and we have shown how to efficiently implement an absorption condition ($c=0$) at an outlet. Numerical tests show that these algorithms are much more accurate than the *ad hoc* methods that are typically used for such problems.

We have tested a multidimensional implementation in a rectangular domain, for which precise numerical solutions are available for comparison. The overall agreement with finite-difference results was excellent, even though the steep concentration gradients in the vicinity of singular corners made for a stringent test of the algorithm. In general we found quadratic convergence in the time step almost everywhere in the domain and linear convergence near the singular points. The stochastic method is not as efficient as finite-difference methods in simple geometries. However, if statistical errors of a few percent are acceptable, such meth-

ods may be viable in irregular geometries.

We have examined several different increment distributions for the random walk. For test purposes a Gaussian distribution is the simplest and the most accurate, but finite-range increments are desirable in complex geometries and are also more efficient. Although finite-range propagators can introduce significant errors near an interface, of order $\sqrt{\Delta t}$ at short times, the errors at long times are smaller. We have found that truncated Gaussian distributions have much smaller errors in the vicinity of an interface than uniformly

sampled increments; discrete increments have even larger errors than uniform distributions.

ACKNOWLEDGMENTS

This work was supported by the U.S. Department of Energy, Chemical Sciences, Geosciences and Biosciences Division, Office of Basic Energy Sciences, Office of Science (Grant No. DE-FG02-98ER14853).

-
- [1] A. Haji-Sheikh and E.M. Sparrow, *J. Heat Transfer* **122**, 121 (1967).
- [2] A.J. Chorin, in *Computing Methods in Applied Science and Engineering*, edited by R. Glowinski and J.L. Lions (North-Holland, Amsterdam, 1980), pp. 229–235.
- [3] Y. Zhu, P.J. Fox, and J.P. Morris, *Int. J. Numer. Anal. Meth. Geomech.* **23**, 881 (1999).
- [4] A.R. Mitchell, in *Computational Techniques and Applications: CTAC-83*, edited by J. Noye and C.A.J. Fletcher (Elsevier, Amsterdam, 1984).
- [5] S.V. Patankar, *Numerical Heat Transfer and Fluid Flow* (McGraw-Hill, New York, 1980).
- [6] Yu.A. Shreider, *The Monte Carlo Method* (Pergamon Press, New York, 1966).
- [7] S.K. Fraley, T.J. Hoffman, and P.N. Stevens, *J. Heat Transfer* **102**, 121 (1980).
- [8] A.F. Ghoniem and F.S. Sherman, *J. Comput. Phys.* **61**, 1 (1985).
- [9] W. Kinzelbach, *Groundwater Flow and Quality Modeling*, edited by E. Custodio *et al.* (Reidel, Dordrecht, 1988), pp. 227–245.
- [10] A.S. Sherman and C.S. Peskin, *SIAM (Soc. Ind. Appl. Math.) J. Sci. Stat. Comput.* **9**, 170 (1988).
- [11] A.L. Fogelson, *J. Comput. Phys.* **100**, 1 (1992).
- [12] M. Abbott, *An Introduction to the Method of Characteristics* (Thames and Hudson, London, 1966).
- [13] J. Douglas, Jr., and T.F. Russell, *SIAM (Soc. Ind. Appl. Math.) J. Numer. Anal.* **19**, 871 (1982).
- [14] S.P. Neuman, *Int. J. Numer. Methods Eng.* **20**, 321 (1984).
- [15] P. Degond and S. Mas-Gallic, *Math. Comput.* **53**, 485 (1989).
- [16] S. Zimmermann, P. Koumoutsakos, and W. Kinzelbach, *Int. J. Numer. Anal. Meth. Geomech.* **173**, 322 (2001).
- [17] C. Zheng and G.D. Bennett, *Applied Contaminant Transport Modeling: Theory and Practice* (Wiley, New York, 1997).
- [18] G.-H. Cottet and P.D. Koumoutsakos, *Vortex Methods. Theory and Practice* (Cambridge University Press, Cambridge, 2000).
- [19] J. Honerkamp, *Stochastic Dynamical Systems* (VCH, New York, 1993).
- [20] P.E. Kloeden and E. Platen, *Numerical Solution of Stochastic Differential Equations*, Applications of Mathematics, Vol. 23 (Springer, New York, 1993).
- [21] H.C. Öttinger, *Stochastic Processes in Polymeric Fluids* (Springer-Verlag, Berlin, 1996).
- [22] H. Risken, *The Fokker-Planck Equation. Methods of Solution and Applications* (Springer, Berlin, 1984).
- [23] S. Chandrasekar, *Rev. Mod. Phys.* **15**, 1 (1943).
- [24] N.G. van Kampen, *Stochastic Processes in Physics and Chemistry* (North-Holland, Amsterdam, 1981).
- [25] I. Ippolito, G. Daccord, E.J. Hinch, and J.P. Hulin, *J. Contam. Hydrol.* **16**, 87 (1994).
- [26] G. Drazer and J. Koplik, *Phys. Rev. E* **63**, 056104 (2001).
- [27] P. Kurowski, I. Ippolito, J.P. Hulin, J. Koplik, and E.J. Hinch, *Phys. Fluids* **6**, 108 (1994).
- [28] T. Rage, Ph.D. thesis, University of Oslo, 1996.
- [29] J. Salles, J.F. Thovert, R. Delannay, L. Prevors, J.L. Aurialt, and P.M. Adler, *Phys. Fluids A* **5**, 2348 (1993).
- [30] R.S. Maier, D.M. Kroll, R.S. Bernard, S.E. Howington, J.F. Peters, and H.T. Davis, *Phys. Fluids* **12**, 2065 (2000).
- [31] M. Zhang and J. Koplik, *Phys. Rev. E* **56**, 4244 (1997).
- [32] R. Verberg and A.J.C. Ladd, *Phys. Rev. E* **65**, 016701 (2002).
- [33] *NAG Fortran Library Manual, Mark 18* (The Numerical Algorithms Group Limited, Oxford, 1997).